Journal of X-Ray Science and Technology 23 (2015) 147–156
DOI 10.3233/XST-150478
IOS Press

A modularly designed fluorescence molecular tomography system for multi-modality imaging

Guohe Wang[a], Bin Zhang[b], Yichen Ding[a], Yun He[b], Jingsong Chen[b], Yanye Lu[a], Xiaoyun Jiang[a], Junwei Shi[b], Jing Bai[b], Qiushi Ren[a,*] and Changhui Li[a,*]
[a]*Department of Biomedical Engineering, Peking University, Beijing, China*
[b]*Department of Biomedical Engineering, Tsinghua University, Beijing, China*

Received 5 May 2014
Revised 9 December 2014
Accepted 5 January 2015

Abstract. Nowadays multi-modality imaging has gained great interest in biology research by offering complementary information. In this paper, a modularly designed fluorescence molecular tomography (FMT) system has been developed, which can be not only used as a standalone imaging device, but also feasibly integrated with other imaging modalities, such as X-ray computed tomography (X-CT), single photon emission computed tomography (SPECT) and positron emission tomography (PET), to perform multi-modality imaging in a sequential manner. The system rotates the CCD camera and the excitation light source in the vertical plane, while the animal is stationed on a horizontally moveable transparent animal holder at its natural prone position. FMT and other imaging modalities are co-registered automatically. Phantom and animal experiments have been carried out to demonstrate the performance of the system. The accurate results show that this innovative flexible FMT system has a great potential to be a powerful tool for the study of small animal disease models.

Keywords: Fluorescence molecular tomography, multi-modality imaging, fluorescence imaging

1. Introduction

Due to the superior sensitivity and specificity, relative ease of use and cheap expense, fluorescence imaging plays a key role in biomedical researches [1–5]. A traditional fluorescence imaging system typically reveals only the two-dimensional (2D) fluorescent emission pattern on the animal surface, lacking the accurate information of spatial distribution of the deep fluorophores [6]. To overcome this limitation, many researchers have been exploring various fluorescence molecular tomography (FMT) (also called fluorescence tomography) methods to resolve the three-dimensional (3D) distribution of the fluorophores since later 1990s [7,8]. Over the past decades, FMT has gained significant progresses and increasing interest in preclinical animal studies [9–13].

*Corresponding authors: Qiushi Ren, Changhui Li, Department of Biomedical Engineering, Peking University, Beijing 100871, China. E-mail: chli@pku.edu.cn; renqsh@coe.pku.edu.cn.

FMT employs the multiple illuminations and detections over different locations of the animal surface, and reveals the fluorescence distribution by solving the inverse problem. Several types of FMT systems have been developed [6,14–23]. Early fiber-based system uses tens to hundreds of optical fibers to convey excitation light and receive fluorescence around the object, which also requires the coupling matching medium [6,14–16]. Although this type has the advantage that no moving part is required during imaging, its complex system setup and coupling requirement limit the application. Another later developed FMT type employs the CCD camera to non-contact acquire fluorescent emission in free space [17–23], which obviously improves the spatial sampling. Recent development of FMT techniques has been taken a step further from the standalone system to multi-modality imaging, such as FMT/X-CT [24–26], FMT/MRI [27,28], and FMT/PET [29,30]. Multi-modality imaging not only presents co-registered complementary information, but also provides important prior information for FMT from other modalities to improve the image reconstruction [31–34]. Here we presented a modular designed FMT system which can not only serve as a standalone FMT instrument, but also especially be feasibly integrated with various imaging modalities, such as FMT/X-CT, FMT/SPECT, FMT/X-CT/SPECT, and etc. In our FMT a rotational module was elaborately designed to rotating the whole imaging system in the vertical plane while keeping the animal stable during the imaging process. Considering the full angle projection without light shielding in FMT and long experiment time in multi-modality imaging, for the first time we used a transparent tube as the animal bed to hold the animal stably in a horizontal position. Our design alleviates body and internal organ movement compared with vertically hanging and rotating animal. When performing multi-modality imaging, a stable one-dimensional translational stage moves the transparent animal holder from FMT to the field of view of other modalities, which avoids animal orientation changing. To fuse the multi-modal images, a simple and automatic registration method was proposed.

In the following, our imaging system and reconstruction algorithm are first introduced. Then we describe experiments in standalone mode and take the FMT/X-CT for the example of multi-modality mode. At last, conclusions and discussions are provided. Our results demonstrate that this FMT system has a great potential for *in vivo* small animal imaging.

2. Methods and imaging system

2.1. Instrumentation

2.1.1. The modularly designed FMT system

The developed FMT system is a non-contact imaging system rotating in a vertical plane, as shown in Fig. 1. It mainly consists of the excitation module, the detection module, the animal holder, the rotational module, and the system control module.

The excitation module contains a Halogen lamp (7ILT250, 7-star, China), an excitation filter wheel (FW102C, Thorlabs Co., USA) and a custom-designed excitation fiber. The Halogen lamp has a continuous spectrum from 300 nm to 2500 nm. By choosing different band-pass filters mounted in the excitation filter wheel, the lamp can excite various fluorescent agents efficiently and conveniently to accomplish the multi-spectral imaging. The input end of the fiber is designed to be a circular shape while its output end is rectangular shape [35]. The filtered light is delivered into the fiber. After passing a cylindrical focusing lens, the light from the fiber finally forms a uniform line-shaped illumination pattern along the longitudinal direction of the animal holder. The width and length of the line-shaped pattern can be controlled by an adjustable slit.

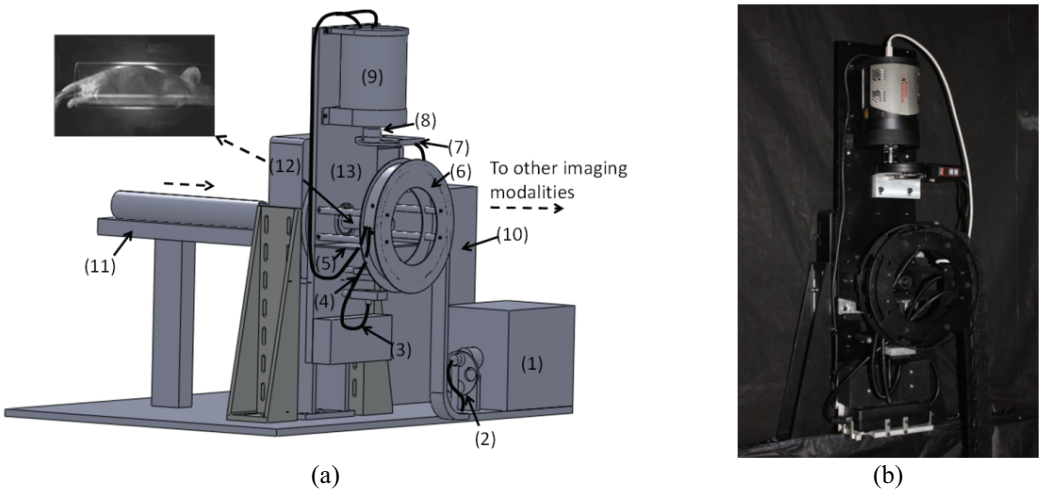

Fig. 1. The FMT system. (a) The schematic of the FMT setup: (1) Halogen lamp (2) Excitation filter wheel (3) Excitation fiber (4) Cylindrical lens (5) Slit (6) Hub disk (7) Emission filter wheel (8) Camera lens (9) CCD camera (10) System control module (11) Translational stage (12) Animal holder (13) Rotational gantry. (b) The photograph of the prototype. (Colours are visible in the online version of the article; http://dx.doi.org/10.3233/XST-150478)

In the detection module, a $-80°$C cooled CCD camera (PIXIS 512B, Princeton Instrument, USA) with 512×512 pixels is placed on the rotational gantry opposite to the excitation fiber. A 35 mm f/1.6 camera lens (C3516-M, Pentax, Japan) is coupled to the CCD. The field of view is 10 cm $\times$ 10 cm, covering the entire trunk of a typical nude mouse. An emission filter wheel (FW102C, Thorlabs Co., USA) is mounted in front of the camera lens, housing up to six filters.

A transparent thin-walled plexi-glass tube is adopted as the animal holder. The animal holder is mounted on a high-precision linear stage (WN250TA300L, Winner Optics, China), which can translate the animal to the field of view of each imaging system. Besides, the animal holder is aligned to position at the center of the rotational gantry, keeping the excitation light always perpendicularly incident onto the surface of the round animal holder during the $360°$ rotation of the gantry, which reduces the refraction of the excitation light caused by the tube.

The rotational module contains the rotational gantry, the hub disk and the drag chain. As shown in Fig. 1, the system has fixed parts and rotational parts. The control module, as well as part of the excitation module including the Halogen lamp, the excitation wheel and one end of the excitation fiber, is stably located outside of the rotational gantry. Since there are both wire cables and the fiber, an elaborately designed hub disk and the drag chain rather than electrical slip ring are adopted for transmitting electric and light from stationary parts to rotational parts. In order to avoid damaging the wire cables and fibers that connect the two parts, both cables and fibers are housed in the drag chain. Then the chain is fixed on a custom-designed hub disk. During the $360°$ rotation of the gantry, the drag train will only wrap around the groove of the hub disk. With long wires and fibers, the gantry can counterclockwise rotate several circles. Combining the rotational module with a line-shaped illumination pattern, the system can facilitate full angle parallel excitation of whole body with single circle of scanning.

To minimize the ambient light interference, the FMT system is covered by light absorbing fabric during the experiment. The filter wheels, rotational gantry, CCD camera, and translational stage are all controlled by the system control module using LabVIEW (LabVIEW 2010, National Instruments, USA).

In order to perform multi-modality imaging, our system allows the animal holder to travel through a

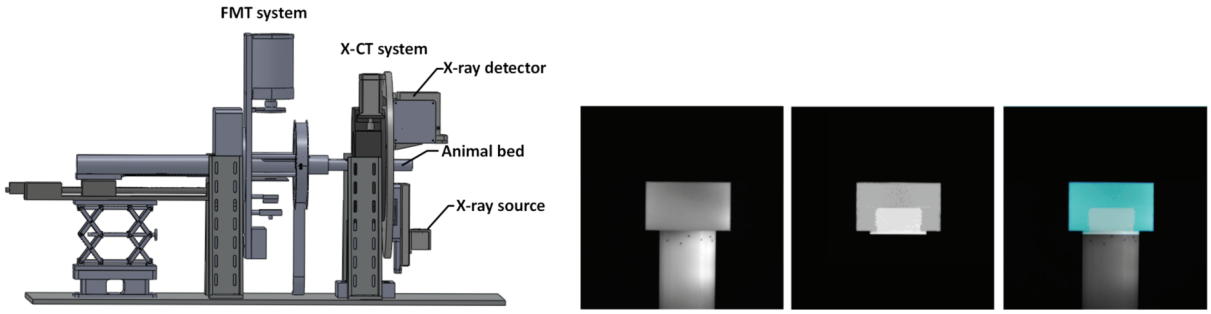

Fig. 2. (a) The schematic design of the FMT/X-CT system (b) the white light image of the solid cube model obtained from FMT at initial angle (c) the X-CT image projection that best matches (b) (d) the fusion of (b) and (c). (Colours are visible in the online version of the article; http://dx.doi.org/10.3233/XST-150478)

hole in the center of the rotational gantry to other imaging modality instruments. Thus multi-modality imaging can be carried out in a sequential way without taking the animal out of the animal holder.

2.1.2. FMT/X-CT systems

In addition, this system is modularly designed to be conveniently integrated with other modal imaging systems. Here we take the FMT/X-CT as the example to demonstrate the multi-modality ability of our FMT. Figure 2(a) presents a schematic diagram of how this FMT system and the X-CT are integrated together in a sequential way. After FMT imaging, the imaged object is transferred to the X-CT system by the translational stage without changing the posture of the object. Based on this design, we have built a prototype of dual-modal system using the developed FMT system and a home-made X-CT system. The X-CT system consists of an X-ray source (XRB011, Spellman High Voltage, USA) with an adjustable voltage of 35–75 kV and a line-type X-ray detector (X-Scan0.4C4, Detection Technology, Finland) with a detection range of 20–160 keV. The X-CT scanning is operated in helical scan mode and the X-CT images are reconstructed using filtered back projection algorithm.

For FMT/X-CT registration, due to the relative low spatial resolution of FMT, it is usually inaccurate to directly co-register the 3D FMT reconstruction result with corresponding X-CT images. Therefore, instead of using FMT reconstruction result, we registered two systems by fitting the 2D white light images of the object obtained by CCD in FMT and its X-CT images. Here we use a solid cube model (3.5 cm $\times$ 3.5 cm $\times$ 2 cm) shown in Fig. 2(b) as a registration marker. There is a cylinder connecting the cube model with the animal bed. The registration procedure consisted of the following steps: (1) FMT, X-CT systems and the animal holder have been first adjusted to be co-axis mechanically. (2) The cube model is imaged by X-CT and the 2D white light image of the model at initial angle is acquired by FMT. (3) The image scaling between FMT and X-CT (ΔS) could be calculated using the pixel size of 2D white light image divided by the pixel size of X-CT image. Then the 2D white light image and the projections of 3D X-CT image are interpolated to have the same pixel size. (4) With the same pixel size, the registration between FMT and X-CT need a rigid transformation with rotation R and translation T:

$$P_{FMT} = R * P_{CT} + T \tag{1}$$

where P_{FMT} and P_{CT} indicate the coordinates of points in FMT and X-CT, respectively. Since FMT, X-CT systems and the animal holder have been adjusted to be co-axis mechanically, there is only rotation

around z-axis (rotation angle θ) and translation along z-axis (t) between FMT and X-CT. Thus R and T are simplified as:

$$R = \begin{bmatrix} \cos\theta & \sin\theta & 0 \\ -\sin\theta & \cos\theta & 0 \\ 0 & 0 & 1 \end{bmatrix}, \quad T = \begin{bmatrix} 0 \\ 0 \\ t \end{bmatrix} \tag{2}$$

t is calculated by

$$t = \overline{Z}_{FMT} - \overline{Z}_{CT} \tag{3}$$

where $\overline{Z}_{FMT}$ and $\overline{Z}_{CT}$ are the mean z coordinates of the upper and lower boundaries of the cube model read from the 2D white light image of FMT and X-CT projections, respectively.

After translational transformation along z-axis, only θ needs to be determined. The initial detector positions of FMT and X-CT are both at the peaks of the gantries as shown in Fig. 2(a). Thus θ between FMT and X-CT should be smaller than 10°. First the 2D white light image of the cube obtained from FMT was binarized to I_{FMT}. Then the X-CT projections ($-10°$ to 10° around the X-CT initial angle, 0.5° interval) were obtained and binarized to I_{CT}. Finally θ is the angle maximizing the matching of I_{FMT} and I_{CT} which can be calculated by counting the number of pixels that are either both zero or both non-zero in I_{FMT} and I_{CT}. The white light image at initial angle of FMT and the best matching X-CT projection are shown in Figs 2(b) and (c), and the fusion of them is shown in Fig. 2(d).

Once the transformation parameters have been determined, FMT and X-CT images can be co-registered straightforwardly by Eq. (1). Aside from FMT/X-CT, this design and the co-registration method can also be applied to other multi-modality systems such as FMT with PET or SPECT, as long as the position of markers can be accurately detected by all the systems.

2.2. FMT image reconstruction algorithm

In continuous wave (CW) mode, the fluorescence migration in highly scattering biological tissues can be modelled using the diffusion equation with the Robin-type boundary condition [36]. With known optical coefficients, the Green's functions $G(r_s, r)$ describing the light transportation due to a source term $S(r_s)$ can be obtained as follows:

$$\begin{cases} -\nabla \cdot [D(r)\nabla G(r_s, r)] + \mu_a(r)G(r_s, r) = S(r_s), & r \in \Omega \\ 2\rho D(r)\dfrac{\partial G(r_s, r)}{\partial \vec{n}} + G(r) = 0, & r \in \partial\Omega \end{cases}, \tag{4}$$

where $D = 1/(3(\mu_a + \mu_s'))$ is the diffusion coefficient, μ_s' and μ_a are the reduced scattering coefficient and the absorption coefficient, Ω is the domain of the imaged object and $\partial\Omega$ is the boundary, $\vec{n}$ denotes the outward normal vector to the boundary, and ρ is a constant depending upon the optical reflective index mismatch at the boundary.

Then the fluorescence signal detected at r_d due to an excitation source at r_s is obtained as follows:

$$\Phi_m(r_s, r_d) = \Theta \int G(r_d, r)x(r)G(r, r_s)dr, \tag{5}$$

where Θ is a calibration factor which accounts for the unknown gain and attenuation factors of the system, x is the unknown fluorescence distribution to be reconstructed.

In this paper, line-shaped excitation light is used, which can effectively excite the fluorescent targets in the entire interested domain [37]. Then the Green's functions $G(r_s, r)$ of line-shaped excitation light can be formulated as follows:

$$G\left(\{r_l\}, r\right) = \int G\left(r_l, r\right) dr_l, \tag{6}$$

where r_l is the point in the line $\{r_l\}$. The Green's functions are computed using the finite element method.

The imaged object is discretized into N_{voxel} 3D voxels. For the total number of N_{data} source-detector pairs, Eq. (5) is transformed into a linear equation with normalized Born approximation [16]:

$$u = \frac{\Phi_m}{\Phi_x} = \frac{\Theta G_m(r_d, r) x(r) G_x(r, r_s) \Delta V}{G_x(r_d, r_s)} = Wx, \tag{7}$$

where Φ_x and Φ_m are the measured excitation and emission respectively, ΔV is the volume of the discretized voxel, u with the size of $N_{data} \times 1$ is the normalized Born approximation of measurements at the surface, W of size $N_{data} \times N_{voxel}$ is the weight matrix, and x of size $N_{voxel} \times 1$ denotes the fluorescence distribution to be reconstructed. Equation (7) is solved by algebraic reconstruction technique (ART) with a relaxation parameter $\lambda = 0.1$ and 200 iterations.

3. Experiments

To evaluate the performance of FMT system in both standalone and multi-modality mode, we carried out phantom and animal experiments. In these experiments, the transparent glass tube (inner diameter 0.24 cm) containing Indocyanine green (ICG, 20 μL with 10 μM) on its tip was used as the fluorophore. Accordingly, the excitation filter (FF01-769/41-25, Semrock Co.) with 769 $\pm$ 20.5 nm passband and the emission filter (FF01-832/37-25, Semrock Co.) with 832 $\pm$ 18.5 nm passband were chosen respectively by controlling filter wheels. The line-shaped illumination beam was adjusted to 1.4 cm in length and 0.1 cm in width. The fluorescence images were collected from 36 projections evenly along the 360° rotation, and at each projection the integration times of the CCD camera were 4 s and 10 s for the phantom and animal experiments, respectively. Besides fluorescence signal detection, the excitation light images were also acquired without any filter (CCD integration time 0.01 s) in both phantom and animal experiments for normalized Born approximation.

3.1. Phantom experiment of the standalone FMT system

To validate our FMT as a standalone system, we have carried out a phantom experiment with two fluorophores in different regions. As shown in Fig. 3(a), two glass tubes containing ICG mentioned above were inserted into a transparent cylindrical holder (2.5 cm diameter). In Z-axis direction the centers of glass tubes were placed at $Z = 3.0$ cm and $Z = 1.4$ cm, and in X-axis direction the two tubes were overlapped. To mimic tissue optical scattering, the holder was filled with 1% intralipid solution. The solution had the absorption coefficient of $\mu_a = 0.02$ cm^{-1} and reduced scattering coefficient of $\mu_s' = 10.0$ cm^{-1} [35]. The 3D geometry of the phantom was reconstructed by the inverse Radon transform method using 36 white light images [38]. A tetrahedral mesh (8287 elements and 13317 nodes) was used for the forward solver, while $25 \times 25 \times 47$ voxels were sampled for the inverse problem within a target

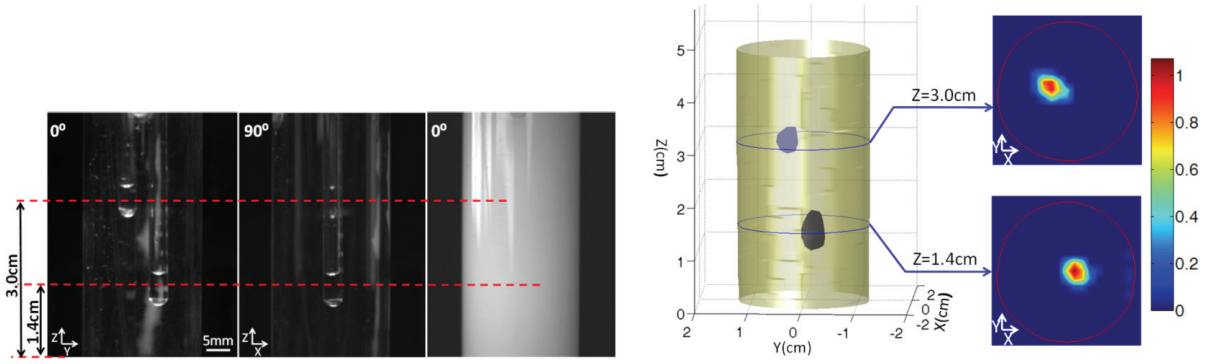

(a) (b)

Fig. 3. Phantom experiment of the standalone FMT. (a) The left and middle images were the real positions of the two tubes in the holder from 0° and 90° projection, respectively. The right was the white image of the phantom after injecting the intralipid solution at 0°, dashed lines depicted the centers of the fluorophores; (b) 3D reconstruction result of the two fluorophores (the left) and the transverse slices (the right) at $Z = 3.0$ cm and $Z = 1.4$ cm. The circles on the transverse images indicate the boundary of the phantom. (Colours are visible in the online version of the article; http://dx.doi.org/10.3233/XST-150478)

volume of 2.5 cm × 2.5 cm × 4.7 cm. For each projection of fluorescence and excitation images, 20 × 23 detectors were considered for reconstruction.

Figure 3(b) shows the reconstructed three-dimensional fluorophore distributions, where the two transverse slices mark the axial positions of the actual fluorophores. The result indicates that both fluorescent targets in different positions are successfully localized in 3D.

3.2. Animal experiment of FMT/X-CT dual-modality imaging

Preliminary animal experiment has been done by the FMT/X-CT system to test the multi-modality capacity. First, the same FMT imaging process as in 3.1 was performed, except that the object geometry was acquired by the more accurate X-CT results. Then the animal holder passed through the hole of the FMT gantry to reach the X-CT system. Third, X-CT scan was performed: The X-ray tube was adjusted to 50 keV and 10 mA, and a helical scan mode (60 scan slices, 1.5 mm helical pitch) was carried out. Finally X-CT provided the surface profile information to FMT for reconstruction.

Animal experiment was conducted using a 23 g BALB/c nude mouse. The mouse was firstly euthanized by CO_2 gas chamber, then immediately a glass tube with 20 μL (10 μM) ICG solution was inserted into the abdominal cavity of the nude mouse from anus. After that, the mouse was fixed in the plexi-glass tube (inner diameter 2.1 cm), as shown in Fig. 4 (d) to be performed with FMT/X-CT imaging. In the FMT reconstruction the initial optical parameters were set as $\mu_a = 0.3\ \text{cm}^{-1}$ and $\mu_s' = 10.0\ \text{cm}^{-1}$ [39]. A tetrahedral mesh (4502 elements and 7080 nodes) was used for the forward solver, while 21 × 21 × 22 voxels were sampled for the inverse problem within a target volume of 2.1 cm × 2.1 cm × 2.2 cm. For each view 10 × 23 detectors were considered for reconstruction. The 3D distributions of the fluorophore in the mouse reconstructed with the X-CT prior surface information are shown in Fig. 4. Figures 4(f)–(h) show the amplitude profiles of the fluorophore by X-CT and FMT along three axes. The location accuracy of FMT are 0.5 mm, 0.3 mm and 0.3 mm along z axis, x axis and y axis respectively which is acceptable considering the ill-posed problem in FMT reconstruction.

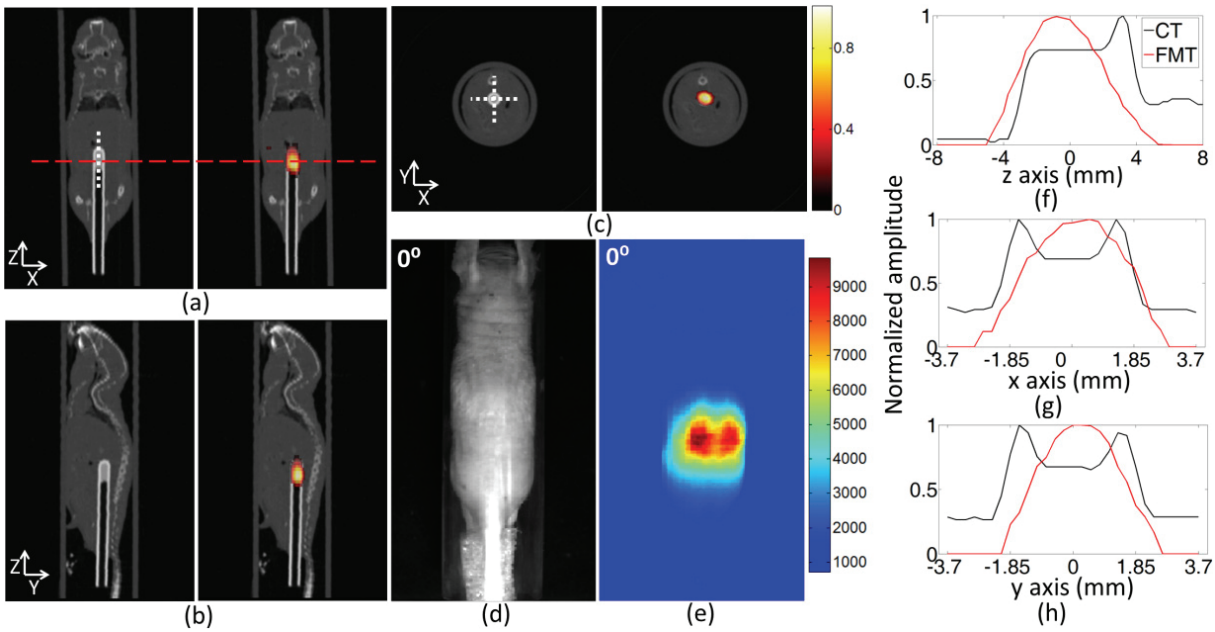

Fig. 4. Mouse experiment of FMT/X-CT. (a), (b) and (c) are the coronal, sagittal and axial X-CT views and the corresponding FMT/X-CT fusion images of the mouse, respectively. The dashed line in (a) indicates the position of the axial view in (c). (d) and (e) are the white and fluorescence images of the mouse at 0°. (f)–(h) compared the normalized amplitude profiles of X-CT and FMT results along different white dotted lines, respectively. (Colours are visible in the online version of the article; http://dx.doi.org/10.3233/XST-150478)

4. Conclusion and discussion

In this paper, we have presented a modularly designed FMT system, which can not only work as a standalone fluorescence imaging system, but also have the capability to be integrated with various imaging modalities to perform multi-modality imaging. The vertical rotational module and transparent animal holder keep the animal in a natural and steady posture during the long imaging process. Phantom and animal experiments in 3.1 and 3.2 have showed that the system accurately reconstructed the fluorophore distributions under both homogeneous and heterogeneous optical backgrounds and that the simple automatic co-registration method was very suitable for multi-modality systems.

There are still several issues and challenges. Refraction may affect both the excitation and emission light propagation when they transmit through the transparent wall of the animal holder. In our current setup, the excitation light has been kept perpendicularly incident on the surface of the animal holder during the 360° rotation to reduce this influence in our system. In future, besides using a holder with thinner wall, algorithms compensating refraction are also under study. Moreover, the FMT result is highly affected by the heterogeneous background optical properties. Although normalized Born approximation method partially corrects heterogeneities, the reconstruction image could be further improved with an inhomogeneous forward model. X-CT or MRI can provide not only the surface morphology which has been used in our FMT reconstruction, but also the internal organ geometries. Integrating FMT with those modalities can help to assign more accurate optical parameters to different tissues. Thus, besides the system development, we will focus on studying new FMT reconstruction algorithms using more prior information from other modalities.

Acknowledgements

This work was sponsored by the National Key Instrumentation Development Project (2011YQ-030114), the National Basic Research Program of China (973 Program, 2011CB707502), the National Basic Research Program of China (973 Program, 2011CB707701), the National Science Foundation of China (61078073) and the National Natural Science Foundation of China (81227901). The authors would like to thank Dr. Yuting Lin (Tu and Yuen Center for Functional Onco Imaging, Department of Radiological Sciences, University of California, Irvine) and Mr. Honghong Zhao (Peking University) for their helpful response to our consultation related to this work.

References

[1] E. Graves, R. Weissleder and V. Ntziachristos, Fluorescence molecular imaging of small animal tumor models, *Current Molecular Medicine* **4** (2004), 419–430.
[2] M. Yang, E. Baranov, P. Jiang, F.-X. Sun, X.-M. Li, L. Li, S. Hasegawa, M. Bouvet, M. Al-Tuwaijri and T. Chishima, Whole-body optical imaging of green fluorescent protein-expressing tumors and metastases, *Proceedings of the National Academy of Sciences* **97** (2000), 1206–1211.
[3] J.E. Bugaj, S. Achilefu, R.B. Dorshow and R. Rajagopalan, Novel fluorescent contrast agents for optical imaging of *in vivo* tumors based on a receptor-targeted dye-peptide conjugate platform, *Journal of Biomedical Optics* **6** (2001), 122–133.
[4] J.H. Lee, H.K. Kim, C. Chandhanayingyong, F.Y.I. Lee and A.H. Hielscher, Non-contact small animal fluorescence imaging system for simultaneous multi-directional angular-dependent data acquisition, *Biomedical Optics Express* **5** (2014), 2301–2316.
[5] J. James, V.M. Murukeshan and L.S. Woh, Integrated Photoacoustic, Ultrasound and fluorescence platform for diagnostic medical imaging-proof of concept study with a tissue mimicking phantom, *Biomedical Optics Express* **5** (2014), 2135–2144.
[6] V. Ntziachristos, Fluorescence molecular imaging, *Annu Rev Biomed Eng* **8** (2006), 1–33.
[7] J. Chang, R.L. Barbour, H.L. Graber and R. Aronson, Fluorescence optical tomography, *Proc SPIE* **2570** (1995), 59–72.
[8] H.B. Jiang, Frequency-domain fluorescent diffusion tomography: A finite-element-based algorithm and simulations, *Applied Optics* **37** (1998), 5337–5343.
[9] V. Ntziachristos, J. Ripoll, L.V. Wang and R. Weissleder, Looking and listening to light: The evolution of whole-body photonic imaging, *Nature Biotechnology* **23** (2005), 313–320.
[10] D. Hyde, R. de Kleine, S.A. MacLaurin, E. Miller, D.H. Brooks, T. Krucker and V. Ntziachristos, Hybrid FMT-CT imaging of Amyloid-β plaques in a murine Alzheimer's disease model, *Neuroimage* **44** (2009), 1304–1311.
[11] H.H. Chen, C. Mekkaoui, H. Cho, S. Ngoy, B. Marinelli, P. Waterman, M. Nahrendorf, R. Liao, L. Josephson and D.E. Sosnovik, Fluorescence tomography of rapamycin-induced autophagy and cardioprotection *in vivo, Circulation: Cardiovascular Imaging* **6** (2013), 441–447.
[12] L. Xi, M. Satpathy, Q. Zhao, W.P. Qian, L. Yang and H.B. Jiang, HER-2/neu targeted delivery of a nanoprobe enables dual photoacoustic and fluorescence tomography of ovarian cancer, *Nanomedicine-Nanotechnology Biology and Medicine* **10** (2014), 669–677.
[13] Q. Zhao, H.B. Jiang, Z.H. Cao, L.L. Yang, H. Mao and M. Lipowska, A handheld fluorescence molecular tomography system for intraoperative optical imaging of tumor margins, *Medical Physics* **38** (2011), 5873–5878.
[14] V. Ntziachristos, C.-H. Tung, C. Bremer and R. Weissleder, Fluorescence molecular tomography resolves protease activity *in vivo*, *Nature Medicine* **8** (2002), 757–761.
[15] V. Ntziachristos and R. Weissleder, Charge-coupled-device based scanner for tomography of fluorescent near-infrared probes in turbid media, *Medical Physics* **29** (2002), 803.
[16] V. Ntziachristos and R. Weissleder, Experimental three-dimensional fluorescence reconstruction of diffuse media by use of a normalized born approximation, *Optics Letters* **26** (2001), 893–895.
[17] E.E. Graves, J. Ripoll, R. Weissleder and V. Ntziachristos, A submillimeter resolution fluorescence molecular imaging system for small animal imaging, *Medical Physics* **30** (2003), 901.
[18] R.B. Schulz, J. Ripoll and V. Ntziachristos, Noncontact optical tomography of turbid media, *Optics Letters* **28** (2003), 1701–1703.
[19] N. Deliolanis, T. Lasser, D. Hyde, A. Soubret, J. Ripoll, V. Ntziachristos, M. Lesaffre, F. Jean, F. Ramaz and A. Boccara, Free-space fluorescence molecular tomography utilizing 360 geometry projections, *Optics Letters* **32** (2007), 382.

[20] H. Meyer, A. Garofalakis, G. Zacharakis, S. Psycharakis, C. Mamalaki, D. Kioussis, E.N. Economou, V. Ntziachristos and J. Ripoll, Noncontact optical imaging in mice with full angular coverage and automatic surface extraction, *Applied optics* **46** (2007), 3617–3627.
[21] Y. Tan and H. Jiang, Diffuse optical tomography guided quantitative fluorescence molecular tomography, *Applied Optics* **47** (2008), 2011–2016.
[22] X. Cao, B. Zhang, F. Liu, X. Wang and J. Bai, Reconstruction for limited-projection fluorescence molecular tomography based on projected restarted conjugate gradient normal residual, *Optics Letters* **36** (2011), 4515–4517.
[23] D. Wang, J. He, H. Qiao, X. Song, Y. Fan and D. Li, High-performance fluorescence molecular tomography through shape-based reconstruction using spherical harmonics parameterization, *PLoS ONE* **9** (2014), e94317.
[24] K.M. Tichauer, R.W. Holt, F. El-Ghussein, Q. Zhu, H. Dehghani, F. Leblond and B.W. Pogue, Imaging workflow and calibration for CT-guided time-domain fluorescence tomography, *Biomedical Optics Express* **2** (2011), 3021.
[25] J. Fu, X. Yang, Y. Meng, Q. Luo and H. Gong, Data preprocessing method for fluorescence molecular tomography using a priori information provided by CT, *Journal of X-ray Science and Technology* **20** (2012), 459–468.
[26] R.B. Schulz, A. Ale, A. Sarantopoulos, M. Freyer, E. Soehngen, M. Zientkowska and V. Ntziachristos, Hybrid system for simultaneous fluorescence and x-ray computed tomography, medical imaging, *IEEE Transactions on* **29** (2010), 465–473.
[27] S.C. Davis, B.W. Pogue, R. Springett, C. Leussler, P. Mazurkewitz, S.B. Tuttle, S.L. Gibbs-Strauss, S.S. Jiang, H. Dehghani and K.D. Paulsen, Magnetic resonance – coupled fluorescence tomography scanner for molecular imaging of tissue, *Review of Scientific Instruments* **79** (2008), 064302-064302-10.
[28] G.A. Gray, C.I. White, A. Thomson, A. Kozak, C. Moran and M.A. Jansen, Imaging the healing murine myocardial infarct *in vivo*: Ultrasound, magnetic resonance imaging and fluorescence molecular tomography, *Experimental Physiology* **98** (2013), 606–613.
[29] A. Garofalakis, A. Dubois, B. Theze, B. Czarny, B. Tavitian and F. Duconge, Fusion of F-18 FDG PET with fluorescence diffuse optical tomography to improve validation of probes and tumor imaging, *Molecular Imaging and Biology* **15** (2013), 316–325.
[30] B. Zhang, S. Liu, F. Liu, X. Zhang, Y. Xu, J. Luo, B. Shan and J. Bai, Simultaneous fluorescence and positron emission tomography for *in vivo* imaging of small animals, *Journal of Biomedical Optics* **16** (2011), 120511–1205113.
[31] P. Mohajerani and V. Ntziachristos, Compression of born ratio for fluorescence molecular tomography/x-ray computed tomography hybrid imaging: Methodology and *in vivo* validation, *Optics Letters* **38** (2013), 2324–2326.
[32] Y. Tan, Z. Cao, H.K. Sajja, M. Lipowska, Y.A. Wang, L. Yang and H. Jiang, DOT corrected fluorescence molecular tomography using targeted contrast agents for small animal tumor imaging, *Journal of X-ray Science and Technology* **21** (2013), 43–52.
[33] K. Radrich, A. Ale, V. Ermolayev and V. Ntziachristos, Improving limited-projection-angle fluorescence molecular tomography using a co-registered x-ray computed tomography scan, *Journal of Biomedical Optics* **17** (2012), 126011–126011.
[34] B. Zhang, S. Liu, X. Cao, F. Liu, X. Wang, J. Luo, B. Shan and J. Bai, Fluorescence tomography reconstruction with simultaneous positron emission tomography priors, *IEEE Transactions on Multimedia* **15** (2013), 1031–1038.
[35] F. Liu, X. Liu, D. Wang, B. Zhang and J. Bai, A parallel excitation based fluorescence molecular tomography system for whole-body simultaneous imaging of small animals, *Annals of Biomedical Engineering* **38** (2010), 3440–3448.
[36] S.R. Arridge, Optical tomography in medical imaging, *Inverse Problems* **15** (1999), R41.
[37] D. Wang, X. Liu and J. Bai, Analysis of fast full angle fluorescence diffuse optical tomography with beam-forming illumination, *Opt Exp* **17** (2009), 21376–21395.
[38] D. Wang, X. Liu, Y. Chen and J. Bai, *In-vivo* fluorescence molecular tomography based on optimal small animal surface reconstruction, *Chinese Optics Letters* **8** (2010), 82–85.
[39] R.B. Schulz, J. Ripoll and V. Ntziachristos, Experimental fluorescence tomography of tissues with noncontact measurements, *Medical Imaging, IEEE Transactions on* **23** (2004), 492–500.